Accepted Manuscript

Non-modal analysis of spectral element methods: Towards accurate and robust large-eddy simulations

Pablo Fernandez, Rodrigo C. Moura, Gianmarco Mengaldo, Jaime Peraire

PII: S0045-7825(18)30586-3
DOI: https://doi.org/10.1016/j.cma.2018.11.027
Reference: CMA 12180

To appear in: *Comput. Methods Appl. Mech. Engrg.*

Received date : 25 April 2018
Revised date : 20 October 2018
Accepted date : 27 November 2018

Please cite this article as: P. Fernandez, R.C. Moura, G. Mengaldo et al., Non-modal analysis of spectral element methods: Towards accurate and robust large-eddy simulations, *Computer Methods in Applied Mechanics and Engineering* (2018), https://doi.org/10.1016/j.cma.2018.11.027

Highlights (for review)

- Introduced non-modal analysis to assess dissipation of spectral element methods (SEM)
- Non-modal analysis shows excellent agreement with large-eddy simulation results
- Non-monotonic dissipation in wavenumber space may lead to stability issues
- Numerical dissipation in discontinuous SEM resembles a subgrid-scale model
- Moderately high orders in discontinuous SEM seem best for large-eddy simulation

Non-modal analysis of spectral element methods: Towards accurate and robust large-eddy simulations

Pablo Fernandez[a,*], Rodrigo C. Moura[b], Gianmarco Mengaldo[c], Jaime Peraire[a]

[a] *Department of Aeronautics and Astronautics, Massachusetts Institute of Technology, USA.*

[b] *Instituto Tecnológico de Aeronáutica (ITA), Brazil*

[c] *Division of Engineering and Applied Science, California Institute of Technology, USA.*

Abstract

High-order spectral element methods (SEM) for large-eddy simulation (LES) are still very limited in industry. One of the main reasons behind this is the lack of robustness of SEM for under-resolved simulations, which can lead to the failure of the computation or to inaccurate results, aspects that are critical in an industrial setting. To help address this issue, we introduce a *non-modal* analysis technique that characterizes the numerical diffusion properties of spectral element methods for linear convection-diffusion problems, including the scales affected by numerical diffusion and the relationship between the amount of numerical diffusion and the level of under-resolution in the simulation. This framework differs from traditional eigenanalysis techniques in that all eigenmodes are taken into account with no need to differentiate them as physical or unphysical. While strictly speaking only valid for linear problems, the non-modal analysis is devised so that it can give critical insights for under-resolved nonlinear problems. For example, why do SEM sometimes suffer from numerical stability issues in LES? And, why do they other times are robust and successfully predict under-resolved turbulent flows even without a subgrid-scale model? The answer to these questions in turns provides crucial guidelines to construct more robust and accurate schemes for LES.

For illustration purposes, the non-modal analysis is applied to the hybridized discontinuous Galerkin methods as representatives of SEM. The effects of the polynomial order, the upwinding parameter and the Péclet number on the so-called *short-term diffusion* of the scheme are investigated. From a non-modal analysis point of view, and for the particular case of hybridized discontinuous Galerkin methods, polynomial orders between 2 and 4 with standard upwinding are well-suited for under-resolved turbulence simulations. For lower polynomial orders, diffusion is introduced in scales that are much larger than the grid resolution. For higher polynomial orders, as well as for strong under/over-upwinding, robustness issues can be expected due to low and non-monotonic numerical diffusion. The non-modal analysis results are tested against under-resolved turbulence simulations of the Burgers, Euler and Navier-Stokes equations. While devised in the linear setting, non-modal analysis successfully predicts the behavior of the scheme in the nonlinear problems considered. Although the focus of this paper is on LES, the non-modal analysis can be applied to other simulation fields characterized by under-resolved scales.

Keywords: Hybridized discontinuous Galerkin, high-fidelity simulation, large-eddy simulation, numerical stability, spectral element methods, under-resolved simulations
2010 MSC: 65M60, 65M70, 76F99

*Corresponding author
Email addresses: pablof@mit.edu (Pablo Fernandez), moura@ita.br (Rodrigo C. Moura), mengaldo@caltech.edu (Gianmarco Mengaldo), peraire@mit.edu (Jaime Peraire)

1. Introduction

The use of computational fluid dynamics (CFD) in industry is severely limited by the inability to accurately and reliably predict complex turbulent flows [76]. This is partly due to the current numerical technologies adopted by industry practitioners, that still rely on steady-tailored techniques in conjunction with low-order numerical methods. In fact, the majority of CFD codes are at most second-order accurate in space and are based on Reynolds-Averaged Navier-Stokes (RANS) equations or, more recently, detached-eddy simulation (DES). The use of high-fidelity computer-aided design is still very limited, with large-eddy simulation (LES) largely confined in the research and development branches of industry, or in academia. However, with the increase in computing power, LES is becoming a feasible technique to underpin the complexity of challenging industrial flows at high-Reynolds numbers, and spectral element methods (SEM) are a competitive candidate to improve the performance of the overall computer-aided workflow [37]. In this paper, we use the term *spectral element methods* to refer to high-order methods with more than one degree of freedom (DOF) per computational cell, such as continuous Galerkin (CG), standard discontinuous Galerkin (DG), hybridized DG, spectral difference (SD) and flux reconstruction (FR) methods. Spectral element methods for large-eddy simulation, including CG [36, 38], standard DG [7, 28, 29, 47, 59, 71, 84, 88], hybridized DG [21, 22], SD [44, 68] and FR [67, 85], are actually emerging as a promising approach to predict complex turbulent flows. SEM allow for high-order discretizations on complex geometries and unstructured meshes. This is critical to accurately propagate small-scale, small-magnitude features, such as in transitional and turbulent flows, over the complex three-dimensional geometries commonly encountered in industrial applications. In addition, SEM are well-suited to emerging computing architectures, including graphics processing units (GPUs) and many-core architectures, due to their high flop-to-communication ratio [1, 2]. The use of spectral element methods for LES is being further encouraged by successful numerical predictions (see references above).

However, a critical step needs to be overcome to take advantage of the favorable properties of SEM for LES, that is the lack of robustness of these methods for under-resolved[1] simulations [48, 46, 89]. From this perspective, the numerical diffusion[2] characteristics of the discretization scheme play a critical role in the robustness, as well as in the accuracy, of under-resolved computations. In particular, it is critical to understand the numerical diffusion introduced by the scheme, including the scales affected by numerical diffusion and the relationship between the amount of numerical diffusion and the *level* of under-resolution in the simulation. These points will help provide an answer on why certain SEM computations suffer from numerical stability issues, while others are robust and successfully predict under-resolved turbulent flows even without a subgrid-scale model [7, 27, 29, 54, 55, 84].

For numerical schemes with more than one DOF per computational cell, such as in spectral element methods, several ways of investigating the diffusion characteristics of the scheme are possible. The most popular technique is the eigensolution analysis; which has been succesfully applied to CG [53], standard DG [4, 32, 33, 45, 50, 52], hybridized DG [56] and FR [51] methods. Eigenanalyses address the diffusion and dispersion characteristics, in wavenumber space, of the discretization of linear propagation-type problems, such as the linear convection or convection-diffusion equation in one dimension. In the SEM context, Fourier modes $\exp(i\kappa x)$, where κ denotes wavenumber, are in general not eigenmodes of the discretization, and are therefore given by the contribution of several eigenmodes. In eigenanalysis, typically all but one of the eigenmodes are dismissed as secondary (or unphysical), and the focus is placed on the so-called primary (or physical) eigenmode [52, 53, 51]. The primary eigenmode is the one that more clearly represents well-resolved Fourier modes (i.e. well-resolved wavenumbers), but the secondary eigenmodes can strongly influence the solution characteristics for wavenumbers near the Nyquist wavenumber. As a consequence, considering only the primary eigenmodes accurately characterizes the behavior of the scheme in well-resolved simulations, but

[1] As is customary, we use the term *under-resolved* to refer to simulations in which the exact solution contains scales that are smaller than the grid Nyquist wavenumber (the so-called subgrid scales) and thus cannot be captured with the grid resolution.

[2] While the terms *diffusion* and *dissipation* are commonly used interchangeably in the literature, in this paper we will reserve the latter for situations in which it is some form of energy that is affected, such as kinetic energy in the nonlinear examples considered.

may fail in under-resolved computations in which scales near the Nyquist wavenumber play an important role, such as in LES. Alternatively, because eigenmodes are decoupled in linear problems, one can consider only the least dissipated eigenmode (which may not be the primary one) to assess the long-term dynamics in linear problems. Since all eigenmodes are coupled in the nonlinear setting, one can only expect however that assessing their combined effect will lead to a better understanding of the behavior of the scheme for nonlinear problems.

As an alternative and complementary approach to eigenanalysis, we are interested in the actual (i.e. non-modal) short-term dynamics of the discretization of the linear convection-diffusion equation. Analyzing the short-term dynamics is motivated by the idea that nonlinear dynamical systems behave similarly to its linearized version during a short period of time, and it is some form of the short-term behavior of the linearized system that is likely to be most informative about the nonlinear dynamics. To this end, we introduce a new analysis framework and refer to it as *non-modal analysis* as it resembles non-modal stability theory[3] [73, 81, 82]. Our non-modal analysis is informative of the behavior of the numerical scheme for time instants immediately after an initial condition, which need not be an eigenmode of the discretization, is prescribed. For this reason, we use the term *short-term* to refer to the behavior of the scheme described by the non-modal analysis framework proposed in this paper. We note that the numerical solution at any time can be thought of as an initial condition for the remaining of the simulation, and this interpretation is particularly useful when employing linear techniques to analyze complex nonlinear systems, such as in large-eddy simulation. In particular, we consider initial conditions consisting of a single Fourier mode to provide insights on the robustness and accuracy of the scheme for LES. Our non-modal analysis does not require Fourier modes to be eigenmodes of the discretization, and reconciles with eigenanalysis whenever they actually are. Although the focus of this paper is on LES, the proposed non-modal analysis can be applied to under-resolved simulations in other fields.

The remainder of the paper is organized as follows. In Section 2, we introduce the non-modal analysis framework and apply it to hybridized discontinuous Galerkin methods. The short-term diffusion characteristics of hybridized DG methods are investigated in this section. In Section 3, we assess how non-modal analysis results extend to the nonlinear setting. To that end, we compare non-modal analysis with numerical results for the Burgers, Euler and Navier-Stokes equations. A discussion on how to devise more robust and accurate numerical schemes using insights from non-modal analysis is presented in Section 4. We conclude the paper with some remarks in Section 5.

2. Non-modal analysis for hybridized DG

We illustrate the non-modal analysis framework by applying it to the hybridized DG methods [64, 22]. To this end, we first derive the hybridized DG discretization of the linear convection-diffusion equation, step by step, to facilitate the understanding of the analysis. The hybridized DG methods are a class of discontinuous Galerkin methods that generalizes the Hybridizable DG (HDG) [15, 63], Embedded DG (EDG) [15, 16] and Interior Embedded DG (IEDG) [21] methods, and are becoming increasingly popular for fluid mechanics [18, 22, 31, 42, 72, 74, 83, 90], solid mechanics [75, 79] and electromagnetism [13, 14, 20, 43, 86, 91] since they lead, for moderately high accuracy orders, to more computationally efficient implementations than standard DG methods [25, 64].

The non-modal analysis framework can be easily extended to other SEM, including SD, FR, CG and standard DG methods. We emphasize that the non-modal analysis framework *can be extended* to other SEM, but the diffusion properties of other SEM will in general be different from those of hybridized DG methods. The diffusion properties of other discontinuous SEM, such as FR and standard DG methods, are expected to be

[3] Non-modal stability theory [73, 81, 82] studies the transient growth of non-modal disturbances in linear dynamical systems (non-modal in the sense that they are not eigenmodes) and was a major breakthrough to characterize nonlinear instabilities by analyzing the short-term behavior of the linearized dynamics.

similar to those of hybridized DG methods due to the upwind stabilization of these methods. More significant differences are expected for continuous SEM, such as CG methods, due to their lack of upwind stabilization. In fact, since standard DG and hybridized DG methods are equivalent for linear convection (see Appendix A), our analysis for pure convection does apply to standard DG. The results for pure convection also carry over to certain types of FR schemes (see [19, 49, 87] for the connections between DG and FR methods). Hybridized DG methods are also equivalent to some instances of standard DG methods for pure diffusion (see [15, 60]).

2.1. Spatial discretization of the linear convection-diffusion equation

We consider the linear convection-diffusion equation with constant coefficients in a one-dimensional domain $\Omega = (-\infty, \infty)$, given by

$$\frac{\partial u}{\partial t} + a\frac{\partial u}{\partial x} = \nu\frac{\partial^2 u}{\partial x^2}, \qquad t \geq 0, \tag{1a}$$

$$u = u_0, \qquad t = 0, \tag{1b}$$

where a is the convection velocity, $\nu \geq 0$ is the diffusion coefficient and $u_0 \in \mathcal{C}^2(\mathbb{R};\mathbb{C})$ is a twice continuously differentiable (possibly complex-valued) initial condition. To discretize Eq. (1) in space by hybridized DG methods, we first rewrite it in the following mixed, conservation form

$$\frac{\partial u}{\partial t} + \frac{\partial f(u,q)}{\partial x} = 0, \qquad t \geq 0, \tag{2a}$$

$$q = \frac{\partial u}{\partial x}, \qquad t \geq 0, \tag{2b}$$

$$u = u_0, \qquad t = 0, \tag{2c}$$

where q is the auxiliary gradient variable and $f(u,q) = a\,u - \nu\,q$ is the flux function. After Ω is partitioned into uniform non-overlapping elements Ω_e of size h, the numerical solution and its gradient in a given element Ω_e are approximated by polynomial expansions of the form

$$u_h|_{\Omega_e} = \sum_{j=0}^{P} \tilde{u}_{h,j}(t)\,\phi_j(\xi(x)), \qquad q_h|_{\Omega_e} = \sum_{j=0}^{P} \tilde{q}_{h,j}(t)\,\phi_j(\xi(x)), \tag{3}$$

where ϕ_j are polynomial basis functions of degree up to P, defined in the reference domain $\Omega_{\text{ref}} = [-1,1]$. A linear mapping relation is assumed between the physical coordinate x in element Ω_e and the coordinate $\xi = \xi(x) \in \Omega_{\text{ref}}$. Multiplying Equations (2a)−(2b) by ϕ_i, integrating over Ω_e, and applying integration by parts leads to

$$\frac{h}{2}\int_{\Omega_{\text{ref}}} \frac{\partial u_h}{\partial t}\phi_i + \left(\widehat{f}_h\phi_i\right)_{\ominus}^{\oplus} = \int_{\Omega_{\text{ref}}} f\frac{\partial \phi_i}{\partial \xi}, \tag{4a}$$

$$\frac{h}{2}\int_{\Omega_{\text{ref}}} q_h\phi_i + \int_{\Omega_{\text{ref}}} u_h\frac{\partial \phi_i}{\partial \xi} = \left(\widehat{u}_h\phi_i\right)_{\ominus}^{\oplus}, \tag{4b}$$

where the symbols $\ominus$ and $\oplus$ denote the left and right boundaries of Ω_e, respectively. As is customary in DG methods, expressions (3) are inserted into (4), which are then required to hold for $i = 0, \ldots, P$. Note that we have introduced the interface quantities $\widehat{f}_h$ and $\widehat{u}_h$. The former is the so-called interelement flux, interface flux or numerical flux, and appears in standard DG methods as well. The latter is particular of hybridized DG methods and is an approximation for the solution u on the element faces that takes the same value on the two elements neighboring the considered interface.

To complete the definition of the hybridized DG scheme, it remains to define the numerical flux $\widehat{f}_h$ and enforce its continuity from the left (L) to the right (R) elements sharing the interface. For convection-diffusion problems, the numerical fluxes are usually defined as [60, 69]

$$\widehat{f}_{h,\ominus} = f(\widehat{u}_{h,\ominus}, q_{h,\ominus}) - \sigma(u_{h,\ominus} - \widehat{u}_{h,\ominus}), \tag{5a}$$

$$\widehat{f}_{h,\oplus} = f(\widehat{u}_{h,\oplus}, q_{h,\oplus}) + \sigma(u_{h,\oplus} - \widehat{u}_{h,\oplus}), \tag{5b}$$

where $\sigma = \beta\,|a|$ is the stabilization constant and $\beta \geq 0$ the so-called upwinding parameter. The case $\beta = 1$ corresponds to standard upwinding, whereas $\beta = 0$ corresponds to centered convective fluxes. Also, $0 < \beta \ll 1$ and $\beta \gg 1$ will be referred to as strong under- and over-upwinding, respectively. Note that no explicit stabilization is used for the diffusive term. Since hybridized DG methods have some form of built-in stabilization for second-order operators [25], this choice of σ is customary for high Reynolds number flows [22, 62, 69] and has been adopted here for consistency with the literature. The flux continuity condition is then given by

$$\widehat{f}^L_{h,\oplus} = \widehat{f}^R_{h,\ominus}. \tag{6}$$

We note that Eq. (6) ensures local conservation regardless of the chosen numerical flux formula. Also, for pure convection and our choice of numerical fluxes, it follows that $\widehat{u}_h = (u^L_{h,\oplus} + u^R_{h,\ominus})/2$ and, furthermore, hybridized and standard DG methods lead to the same numerical solution (see Appendix A). This does not hold in general when diffusion is taken into account (i.e. when $\nu > 0$); in which case $\widehat{u}_h$ is only given implicitly from the flux continuity at interfaces, namely,

$$a\widehat{u}_h - \nu q^L_{h,\oplus} + \sigma(u^L_{h,\oplus} - \widehat{u}_h) = au_h - \nu q^R_{h,\ominus} - \sigma(u^R_{h,\ominus} - \widehat{u}_h), \tag{7}$$

where $q^L_{h,\oplus}$ and $q^R_{h,\ominus}$ in turn depend on the values of $\widehat{u}_h$ at two other interfaces via (4b).

To simplify the analysis, we rewrite the hybridized DG discretization in matrix notation. To that end, we note that

$$u_{h,\ominus} = \sum_{j=0}^{P} \tilde{u}_{h,j}\,\phi_j(-1), \qquad q_{h,\ominus} = \sum_{j=0}^{P} \tilde{q}_{h,j}\,\phi_j(-1), \tag{8a}$$

$$u_{h,\oplus} = \sum_{j=0}^{P} \tilde{u}_{h,j}\,\phi_j(+1), \qquad q_{h,\oplus} = \sum_{j=0}^{P} \tilde{q}_{h,j}\,\phi_j(+1), \tag{8b}$$

and introduce the vectors $\tilde{u}_h = \{\tilde{u}_0, \ldots, \tilde{u}_P\}^T$, $\tilde{q} = \{\tilde{q}_0, \ldots, \tilde{q}_P\}^T$, $\tilde{\phi}_\oplus = \{\tilde{\phi}_0(+1), \ldots, \tilde{\phi}_P(+1)\}^T$ and $\tilde{\phi}_\ominus = \{\tilde{\phi}_0(-1), \ldots, \tilde{\phi}_P(-1)\}^T$. The flux continuity condition (6) then can be expressed as

$$\widehat{u}_h = \frac{1}{2}\left(\tilde{\phi}^T_\oplus \tilde{u}^L_h + \tilde{\phi}^T_\ominus \tilde{u}^R_h\right) + \frac{\nu}{2\sigma}\left(\tilde{\phi}^T_\ominus \tilde{q}^R_h - \tilde{\phi}^T_\oplus \tilde{q}^L_h\right). \tag{9}$$

Likewise, the auxiliary equation (4b) can be written as

$$\frac{h}{2} M \tilde{q}_h + D\tilde{u}_h = \tilde{\phi}_\oplus \widehat{u}_{h,\oplus} - \tilde{\phi}_\ominus \widehat{u}_{h,\ominus}, \tag{10}$$

where M and D are the mass matrix and differentiation matrix (also referred to as convection matrix in the finite element community) defined as

$$M_{ij} = \int_{\Omega_{\text{ref}}} \phi_i\,\phi_j, \qquad D_{ij} = \int_{\Omega_{\text{ref}}} \frac{\partial \phi_i}{\partial \xi}\,\phi_j. \tag{11}$$

Finally, Eq. (4a) becomes

$$\frac{h}{2} M \frac{d\tilde{u}_h}{dt} + \tilde{\phi}_\oplus \widehat{f}_{h,\oplus} - \tilde{\phi}_\ominus \widehat{f}_{h,\ominus} = aD\tilde{u}_h - \nu D\tilde{q}_h, \tag{12}$$

with

$$\widehat{f}_{h,\ominus} = a\widehat{u}_{h,\ominus} - \nu\tilde{\phi}_{\ominus}^T\tilde{q}_h - \sigma(\tilde{\phi}_{\ominus}^T\tilde{u}_h - \widehat{u}_{h,\ominus}), \tag{13a}$$

$$\widehat{f}_{h,\oplus} = a\widehat{u}_{h,\oplus} - \nu\tilde{\phi}_{\oplus}^T\tilde{q}_h + \sigma(\tilde{\phi}_{\oplus}^T\tilde{u}_h - \widehat{u}_{h,\oplus}). \tag{13b}$$

Note that (9) is a scalar equation written from the point of view of a given interface, whereas (10) and (12) are vector equations written from the viewpoint of an arbitrary element Ω_e of size h.

At this point, it is convenient to eliminate $\tilde{q}_h$ from the formulation and work with the variables $\tilde{u}_h$ and $\widehat{u}_h$ only. To this end, we use (10) to obtain $\tilde{q}_h$ as a function of $\tilde{u}_h$ and $\widehat{u}_h$, and then substitute the resulting expression into (9) and (12). The former substitution leads, after some algebra, to

$$\left(\bar{\sigma} + \frac{m_{\ominus}^{\ominus}}{\mathrm{Pe}} + \frac{m_{\oplus}^{\oplus}}{\mathrm{Pe}}\right)\widehat{u}_h - \frac{m_{\oplus}^{\ominus}}{\mathrm{Pe}}\widehat{u}_{h,\ominus}^L - \frac{m_{\ominus}^{\oplus}}{\mathrm{Pe}}\widehat{u}_{h,\oplus}^R = \tilde{\phi}_{\oplus}^T B_{\oplus}\tilde{u}_h^L + \tilde{\phi}_{\ominus}^T B_{\ominus}\tilde{u}_h^R, \tag{14}$$

where $\bar{\sigma} = \sigma/|a|$ is a non-dimensional stabilization parameter and Pe denotes the cell Péclet number $\mathrm{Pe} = |a|h/\nu$. Note $\bar{\sigma} = \beta$ for our choice of stabilization. Moreover, the following scalar constants 'm'

$$m_{\ominus}^{\ominus} = \tilde{\phi}_{\ominus}^T M^{-1}\tilde{\phi}_{\ominus}, \qquad m_{\oplus}^{\ominus} = \tilde{\phi}_{\oplus}^T M^{-1}\tilde{\phi}_{\ominus}, \qquad m_{\ominus}^{\oplus} = \tilde{\phi}_{\ominus}^T M^{-1}\tilde{\phi}_{\oplus}, \qquad m_{\oplus}^{\oplus} = \tilde{\phi}_{\oplus}^T M^{-1}\tilde{\phi}_{\oplus}, \tag{15}$$

and matrices

$$B_{\ominus} = \left(\frac{\bar{\sigma}}{2}I - \frac{M^{-1}D}{\mathrm{Pe}}\right), \qquad B_{\oplus} = \left(\frac{\bar{\sigma}}{2}I + \frac{M^{-1}D}{\mathrm{Pe}}\right), \tag{16}$$

have been introduced in (14). Note that Eq. (14) links the solution vectors $\tilde{u}_h$ on two adjacent elements (Ω_L and Ω_R) with the three interface variables $\widehat{u}_h$ corresponding to the boundaries of these elements.

The second substitution, namely inserting $\tilde{q}_h$ from (10) into (12), and using also Equation (13) for the numerical fluxes, yields

$$\frac{h}{2a}M\frac{d\tilde{u}_h}{dt} + A\tilde{u}_h - A_{\ominus}\tilde{\phi}_{\ominus}\widehat{u}_{h,\ominus} + A_{\oplus}\tilde{\phi}_{\oplus}\widehat{u}_{h,\oplus}, \tag{17}$$

where

$$A = \left(\Phi_{\ominus}^{\ominus} - \Phi_{\oplus}^{\oplus}\right) + \left(\frac{2N}{\mathrm{Pe}} - I\right)D, \tag{18a}$$

$$A_{\ominus} = (\bar{\sigma} + 1)\,I - \frac{2N}{\mathrm{Pe}}, \qquad A_{\oplus} = (\bar{\sigma} - 1)\,I + \frac{2N}{\mathrm{Pe}}, \tag{18b}$$

and

$$\Phi_{\ominus}^{\ominus} = \varphi_{\ominus}\tilde{\phi}_{\ominus}^T, \qquad \Phi_{\oplus}^{\oplus} = \tilde{\phi}_{\oplus}\tilde{\phi}_{\oplus}^T, \tag{19a}$$

$$N = \left(\Phi_{\oplus}^{\oplus} - \Phi_{\ominus}^{\ominus} - D\right)M^{-1}. \tag{19b}$$

Note that Eq. (17) links the solution vector $\tilde{u}_h$ and its time derivative to the two interface variables $\widehat{u}_h$ at the boundaries of the considered element.

The hybridized DG discretization of the linear convection-diffusion equation (1) in matrix notation is given by Equations (9), (10) and (12), which are required to hold in all elements and all faces. Equations (14) and (17) are an equivalent formulation in terms of $\tilde{u}_h$ and $\widehat{u}_h$ only. Both formulations need to be further equipped with the discretized version of the initial condition (2c), i.e. $\tilde{u}_h(t=0) = \tilde{u}_{h,0}$, where the right-hand side is the vector of coefficients of the Galerkin projection of u_0 and is given by

$$\tilde{u}_{h,0} = M^{-1}d, \tag{20}$$

where we have introduced the vector

$$d_j = \int_{\Omega_{\mathrm{ref}}} u_0\,\phi_j. \tag{21}$$

We note that all the methods within the hybridized DG family, including Hybridizable DG, Embedded DG and Interior Embedded DG, reduce to the same scheme in one-dimensional problems, and therefore no difference between them has been made here.

2.2. Non-modal analysis formulation

Like in previous works [50, 51, 52, 53], we focus on the analysis of diffusion, which is more relevant and usually dominates dispersion errors in under-resolved turbulence simulations [4, 32, 45, 52]. In particular, we are concerned about the short-term diffusion properties, in wavenumber space, of the hybridized DG discretization of Eq. (1). That is, if the initial condition is a single Fourier mode $u_0 \propto \exp(i\kappa x)$, where $\kappa \in \mathbb{R}$ denotes the wavenumber, how does the magnitude of the numerical solution evolve over time, and in particular right after $t = 0$? To this end, we define the short-term diffusion as

$$\varpi^* := \left. \frac{d \log ||u_h||}{d\tau^*} \right|_{\tau^*=0}, \tag{22}$$

where $||\cdot||$ denotes the $L^2(\mathbb{R})$ norm and $\tau^* = \tau\,(P+1) = t\,a\,(P+1)/h$ is a non-dimensional time based on the convection time between degrees of freedom. Note that we define the distance between degrees of freedom as $h^* = h/(P+1)$ and that $\tau^* = 1$ is the time it takes for a flow with speed a to travel a single DOF. The $*$ superscript, such as in ϖ^*, τ^* and h^*, is used to indicate that a $(P+1)$ factor has been applied to account for the $P+1$ degrees of freedom per element. Also, we note that Eq. (22) can be rewritten as

$$\varpi^* = \lim_{\tau^* \downarrow 0} \frac{1}{\tau^*} \log \left(\frac{||u_h||}{||u_{h,0}||} \right), \tag{23}$$

which some readers may find easier to interpret. As we shall see, ϖ^* depends on the wavenumber κ, the modified Péclet number $\mathrm{Pe}^* = |a|\,h^*/\nu = \mathrm{Pe}/(P+1)$ and the details of the hybridized DG scheme, such as the polynomial order P and the upwinding parameter β.

Intuitively, ϖ^* informs of the decay rate of the numerical solution, per *unit convection time between degrees of freedom*, at early times, starting from the initial condition $\exp(i\kappa x)$. In particular,

$$||u_h(\tau^*)|| \approx ||u_{h,0}|| \exp(\varpi^* \tau^*) \tag{24}$$

at early times, and thus $\exp(\varpi^*)$ can be considered as a *damping factor per DOF crossed*.

Next, we derive an explicit expression for ϖ^*. It can be shown[4] that if $u_0 \propto \exp(i\kappa x)$, then the relations

$$\tilde{u}_h^L = \tilde{u}_h \exp(-i\kappa h), \qquad \tilde{u}_h^R = \tilde{u}_h \exp(+i\kappa h), \tag{25a}$$

$$\widehat{u}_{h,\ominus} = \widehat{u}_{h,\oplus} \exp(-i\kappa h), \tag{25b}$$

hold for all elements and all times. Similarly to the notation adopted above for the elements neighboring an interface, we use the superscripts L and R in (25a) to denote the left and right neighboring elements of a given element. The wave-like behavior of the numerical solution allows reducing the dimensionality of the problem from countably many (infinite) degrees of freedom to $P+1$ degrees of freedom, and this in turn makes our non-modal analysis possible. In particular, it now follows from Equations (14) and (25b) that

$$\widehat{u}_h = \left(\tilde{\phi}_\oplus^T B_\oplus \tilde{u}_h^L + \tilde{\phi}_\ominus^T B_\ominus \tilde{u}_h^R \right) b^{-1}, \tag{26}$$

where $b = b(\kappa h; \mathrm{Pe}, P, \sigma)$ is a scalar defined as

$$b = \bar{\sigma} + \left(m_\ominus^\ominus - m_\oplus^\ominus \exp(-i\kappa h) - m_\ominus^\oplus \exp(+i\kappa h) + m_\oplus^\oplus \right) \mathrm{Pe}^{-1}. \tag{27}$$

[4] The Galerkin projection of $\exp(i\kappa x)$ trivially features this wave-like behavior, and thus (25a) holds at $t = 0$. Equation (25b) at $t = 0$ then follows from (14). Since Equations (25) are satisfied at $t = 0$, it follows from (28) (which holds at any given time under the previous assumptions) that they are also satisfied at all subsequent times $t \geq 0$.

Inserting (25a) and (26) into (17), one finally obtains

$$\frac{h}{a}\frac{d\tilde{u}_h}{dt} = \tilde{Z}_h \tilde{u}_h, \tag{28}$$

where $\tilde{Z}_h = \tilde{Z}_h(\kappa h; \mathrm{Pe}^*, P, \bar{\sigma})$ is a square matrix given by

$$\tilde{Z}_h = 2b^{-1}M^{-1}\big(A_\ominus \Phi_\ominus^\ominus B_\ominus + A_\ominus \Phi_\oplus^\ominus B_\oplus \exp(-i\kappa h) + A_\oplus \Phi_\ominus^\oplus B_\ominus \exp(+i\kappa h) + A_\oplus \Phi_\oplus^\oplus B_\oplus - Ab\big), \tag{29}$$

with $\Phi_\ominus^\ominus$ and $\Phi_\oplus^\oplus$ given by (19a), and

$$\Phi_\oplus^\ominus = \tilde{\phi}_\ominus \tilde{\phi}_\oplus^T, \qquad \Phi_\ominus^\oplus = \tilde{\phi}_\oplus \tilde{\phi}_\ominus^T \tag{30}$$

Since ϖ^* is independent of the choice of basis, we assume without loss of generality that ϕ_j is the orthonormal Legendre polynomial of degree j in $\Omega_{\mathrm{ref}} = [-1, 1]$; in which case we can obtain a closed-form expression for ϖ^*. Combining Equations (22) and (28), using inner product properties, orthonormality of Legendre polynomials and the wave-like behavior of the numerical solution, it follows that

$$\begin{aligned}
\varpi^* &= \frac{d\log||u_h||}{d\tau^*}\bigg|_{\tau^*=0} = \frac{1}{||u_h||}\frac{d||u_h||}{d\tau^*}\bigg|_{\tau^*=0} = \frac{h^*}{a}\frac{1}{(\tilde{u}_h^\dagger \tilde{u}_h)^{1/2}}\frac{d\,(\tilde{u}_h^\dagger \tilde{u}_h)^{1/2}}{dt}\bigg|_{t=0} \\
&= \frac{h^*}{2a}\frac{1}{\tilde{u}_h^\dagger \tilde{u}_h}\left(\frac{d\tilde{u}_h^\dagger}{dt}\tilde{u}_h + \tilde{u}_h^\dagger \frac{d\tilde{u}_h}{dt}\right)\bigg|_{t=0} = \frac{1}{2}\frac{1}{P+1}\frac{\tilde{u}_{h,0}^\dagger \tilde{Z}_h^\dagger \tilde{u}_{h,0} + \tilde{u}_{h,0}^\dagger \tilde{Z}_h \tilde{u}_{h,0}}{\tilde{u}_{h,0}^\dagger \tilde{u}_{h,0}} \\
&= \frac{1}{P+1}\,\mathbb{R}e\left[\frac{\tilde{u}_{h,0}^\dagger \tilde{Z}_h \tilde{u}_{h,0}}{\tilde{u}_{h,0}^\dagger \tilde{u}_{h,0}}\right],
\end{aligned} \tag{31}$$

where the $\dagger$ superscript denotes conjugate transpose and $\mathbb{R}e$ the real part of a complex number. Note that the value of ϖ^* is independent of the amplitude of the Fourier mode. Taking $u_0 = \exp(i\kappa x)$, it follows that $\tilde{u}_{h,0} = \alpha = \alpha(\kappa h)$ with

$$\alpha_0 = \sqrt{2}\,\frac{\sin z}{z}, \qquad \alpha_1 = \frac{i\sqrt{6}}{z}\left(\frac{\sin z}{z} - \cos z\right), \tag{32a}$$

and, for $j \geq 1$,

$$\alpha_{j+1} = \frac{\sqrt{4j+6}}{z}\left(m_j \sin z + i\left(\frac{\sin z}{z} - \cos z\right)m_{j+1} + i\sum_{k=1}^{j}\sqrt{k+1/2}\,m_{j+k+1}\,\alpha_k\right), \tag{32b}$$

where $z = \kappa h/2$ and $m_j = \mathrm{mod}(j, 2)$ is the modulus of j after division by two. Equations (32) hold for orthonormal Legendre polynomials and are presented in [52]. Equations (29), (31) and (32) provide a closed-form expression for $\varpi^* = \varpi^*(\kappa h; \mathrm{Pe}^*, P, \bar{\sigma})$.

We note that $\tilde{Z}_h$ is the same matrix (up to complex sign) as that in eigenanalysis [56]. The difference between eigenanalysis and our non-modal analysis is that the former is concerned about the modal behavior (i.e. the eigenvalues and eigenmodes) of $\tilde{Z}_h$, whereas we are concerned about its non-modal behavior (i.e. we consider the contribution of all the eigenmodes for each wavenumber), and in particular about its non-modal short-term dynamics. Also, our definition of short-term diffusion ϖ^* is consistent with the definition of diffusion introduced in eigenanalysis [52]: If the Fourier mode is an eigenmode of $\tilde{Z}_h$, as it is the case for $P = 0$, then $(P+1)\,\varpi^*$ coincides with the real part of the corresponding eigenvalue, and non-modal analysis reconciles with eigenanalysis. Similarly, if our evaluation is applied to the primary eigenmodes (instead of to the Fourier modes as described above), our results will match the primary eigencurves in [56].

Remark 1. Strictly speaking, Equations (22) and (23) should read as

$$\varpi^* := \lim_{n\to\infty} \left. \frac{d \log \left|\left|\chi_{[-n,n]}\, u_h\right|\right|}{d\tau^*} \right|_{\tau^*=0}, \qquad \varpi^* = \lim_{n\to\infty} \lim_{\tau^*\downarrow 0} \frac{1}{\tau^*} \log \left(\frac{\left|\left|\chi_{[-n,n]}\, u_h\right|\right|}{\left|\left|\chi_{[-n,n]}\, u_{h,0}\right|\right|} \right), \tag{33}$$

respectively, where $\chi_{[-n,n]}$ denotes the indicator function of $[-n,n]$, in order for the norms and thus ϖ^* to be well-defined. A limiting process is also required, and intentional abuse of notation is used, when dealing with $||u_h||$ elsewhere.

Remark 2. Non-modal analysis is a linear technique and does not capture differences between numerical schemes that reduce to the same scheme in the linear constant-coefficient case. For example, stabilization mechanisms that vanish for linear constant-coefficient problems, such as split forms [11, 30, 39, 89] and entropy-stable numerical fluxes [26], cannot be compared with the non-modal analysis framework. In these cases, non-modal analysis predicts the same diffusion characteristics and actual simulations are needed to assess further (nonlinear) differences. Stabilization techniques that do not vanish for linear constant-coefficient problems, such as polynomial dealiasing [48, 89] and spectral vanishing viscosity [45, 53], can however be directly analyzed by non-modal analysis.

2.3. Non-modal analysis results

We present the non-modal analysis results through the so-called short-term diffusion curves. For given Pe^*, P and β, the short-term diffusion curves show ϖ^* (y axis) as a function of the non-dimensional wavenumber $\kappa h^* = \kappa h/(P+1)$ (x axis). The left limit of the x axis in Figures 1, 2 and 3 corresponds to the constant mode $\kappa = 0$, and the right limit to the grid Nyquist wavenumber, defined as $\kappa_N = \pi/h^*$, and thus $\kappa_N h/(P+1) = \pi$. The exact diffusion curves are indicated with dashed lines. The short-term diffusion curves satisfy the symmetry condition $\varpi^*(\kappa h^*) = \varpi^*(-\kappa h^*)$ but, unlike the eigencurves [4, 45, 52], they do not satisfy the periodicity condition $\varpi^*(\kappa h^*) = \varpi^*(\kappa h^* + 2\pi\ell)$, $\ell \in \mathbb{Z}$.

Before presenting the short-term diffusion curves, we briefly discuss how these curves *should look* from the perspectives of robustness and accuracy. For robustness purposes, monotonic ($d\varpi^*/d\kappa \leq 0$) and slowly-varying curves are preferred, particularly for nonlinear systems due to the nonlinear interactions between wavenumbers. Regarding accuracy, the short-term diffusion should agree as much as possible with the exact diffusion curve in the case of well-resolved simulations, such as in direct numerical simulation (DNS) of turbulent flows. However, for under-resolved computations of systems featuring a kinetic energy cascade, such as in LES, additional diffusion is desired, particularly at large wavenumbers, in order for the eddy-viscosity effect of the missing scales [10, 40, 41] to be accounted for by the numerics. Also for robustness purposes, additional numerical diffusion at large wavenumbers is beneficial to provide further regularization and avoid energy accumulation at the smallest resolved scales. These considerations are based on *a priori* knowledge and *a posteriori* insights from the numerical results in Section 3.

2.3.1. Effect of the polynomial order

Figure 1 shows the short-term diffusion curves as a function of the polynomial order for standard upwinding $\beta = 1$ in convection dominated $\mathrm{Pe}^* = 10^3$ (left) and diffusion-dominated $\mathrm{Pe}^* = 0.1$ (right) regimes. The exact solution of the convection-diffusion equation is shown in dashed black line.

For convection-dominated flows, high polynomial orders lead to non-monotonic short-term diffusion characteristics. In particular, very small diffusion is introduced at some specific wavenumbers. As discussed before and shown by the numerical results in Sections 3.1 and 3.2, this may lead to nonlinear instabilities. Also, we recall that some amount of numerical diffusion near κ_N (preferably monotonic in wavenumber space) is desired, both for accuracy and robustness, in under-resolved turbulence simulations to replicate the dissipation that takes place in the subgrid scales. The short-term diffusion properties that are better suited, both in terms of accuracy per DOF and robustness, for convection-dominated under-resolved turbulence

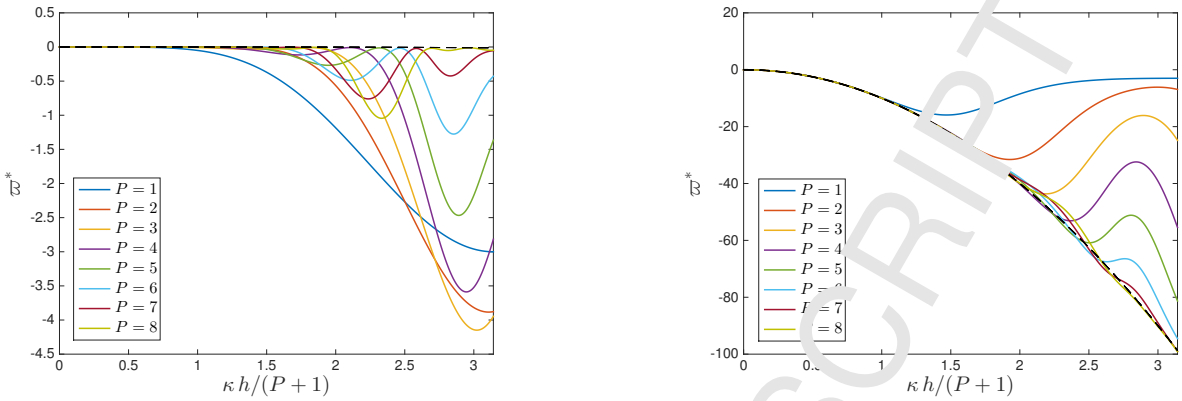

Figure 1: Short-term diffusion curves as a function of the polynomial order for $\beta = 1$ in convection-dominated $\mathrm{Pe}^* = 10^3$ (left) and diffusion-dominated $\mathrm{Pe}^* = 0.1$ (right) regimes. The exact solution of the convection-diffusion equation is shown in dashed black line. Note a different scale in the y axis is used for each figure.

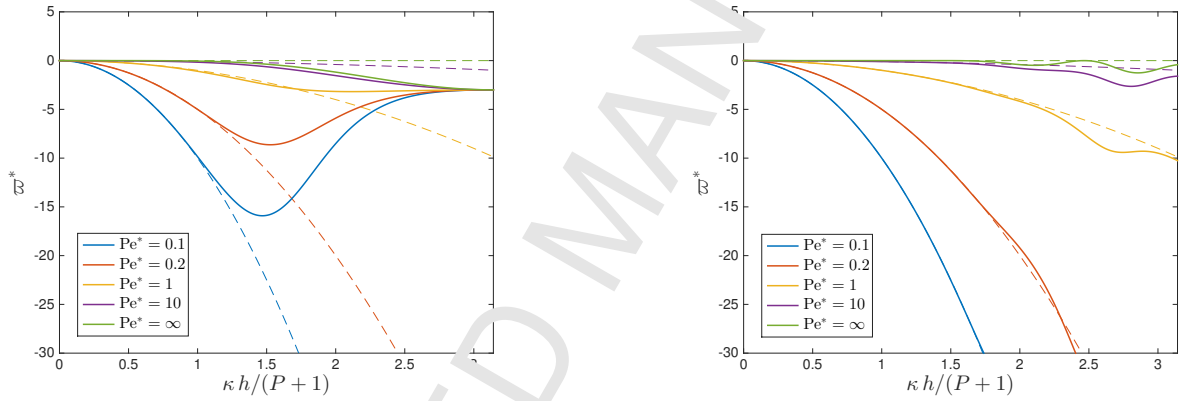

Figure 2: Short-term diffusion curves as a function of the Péclet number for standard upwinding $\beta = 1$ and polynomial orders $P = 1$ (left) and $P = 6$ (right). The exact solution of the convection-diffusion equation is shown in dashed lines.

simulations, seem to be those for polynomial orders $P = 2$, 3 and 4. For $P = 1$, diffusion is introduced at scales that are much larger than the Nyquist wavenumber. We note that convection-dominated, from the cell Péclet number perspective, is the regime most commonly encountered in large-eddy simulation. For diffusion-dominated problems, higher P improves both accuracy per degree of freedom and robustness.

2.3.2. Effect of the Péclet number

Figure 2 shows the short-term diffusion curves as a function of the Péclet number for standard upwinding $\beta = 1$ with polynomial orders $P = 1$ (left) and $P = 6$ (right). The exact solution of the convection-diffusion equation is shown in dashed lines. As noted in the polynomial order study, high P schemes are better suited to diffusion-dominated problems, both in terms of accuracy and robustness. As for low polynomial orders, moderately high wavenumbers are poorly resolved regardless of the Péclet number. Robustness of low P schemes seems to improve in the convection-dominated regime.

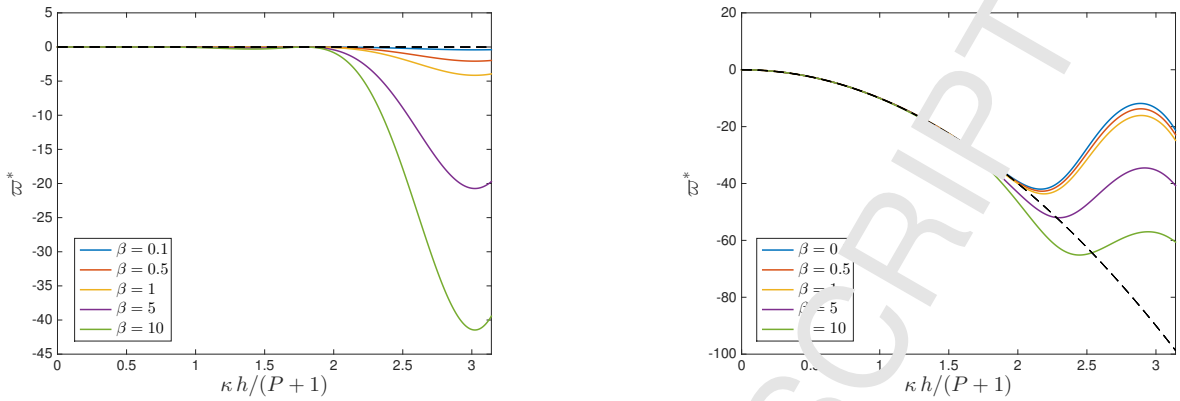

Figure 3: Short-term diffusion curves as a function of the upwinding parameter for $P = 3$ in convection-dominated $\mathrm{Pe}^* = 10^3$ (left) and diffusion-dominated $\mathrm{Pe}^* = 0.1$ (right) regimes. The exact solution of the convection-diffusion equation is shown in dashed black line. Note a different scale in the y axis is used for each figure.

2.3.3. Effect of the upwinding parameter

Figure 3 shows the short-term diffusion curves as a function of the upwinding parameter for $P = 3$ in convection-dominated $\mathrm{Pe}^* = 10^3$ (left) and diffusion-dominated $\mathrm{Pe}^* = 0.1$ (right) regimes. The exact solution of the convection-diffusion equation is shown in dashed black line. Note that, in compressible flow simulations, the case $\beta > 1$ is obtained with Riemann solvers that are based on the maximum-magnitude eigenvalue of the Jacobian matrix of the Euler fluxes, such as the Lax-Friedrichs and the HLL solvers [80]. This is so because in such cases the advection eigenspeed is replaced by the acoustic one in the momentum equations, leading to an upwinding factor $\beta \approx 1 + \mathrm{Ma}^{-1}$. This results in a strong over-upwinding for low Mach number flows, as demonstrated in recent studies [27, 50, 55].

For convection-dominated regimes, strong under/over-upwinding is to be avoided as it causes dissipation at large wavenumbers to rise too slow/fast. The former leads to a lack of small-scale regularization, and the latter causes the bottleneck phenomenon and its associated energy bump, detrimental to both solution quality and numerical stability [55]. Nevertheless, it may be the case that a controlled level of under/over-upwinding may be useful for certain simulations, e.g. when the eddy-viscosity effect of the missing scales is not represented correctly by the standard upwind condition. For diffusion-dominated problems, the scheme benefits form over-upwinding; which is not completely surprising since no explicit stabilization has been used for the diffusion operator.

3. Application to nonlinear problems

To assess how the nodal analysis results extend to the nonlinear setting, we apply it to the Burgers, Euler and Navier-Stokes equations. One-dimensional and three-dimensional examples are considered. We note that hybridized DG methods require solving a system of equations at every time step regardless of whether the time integration scheme is explicit or implicit, see e.g. [24, 25, 60]. For this reason, and due to their superior stability properties, we consider implicit time integration methods in the numerical examples.

3.1. Application to the Burgers equation

3.1.1. Problem description

We consider the following one-dimensional forced Burgers turbulence problem [1?]

$$\frac{\partial u}{\partial t} + \frac{1}{2}\frac{\partial u^2}{\partial x} = \frac{A_F}{\sqrt{\Delta t}} \sum_{N \in \mathbb{N}_F} \frac{\sigma_N(t)}{\sqrt{|N|}} \exp\left(i \frac{2\pi N}{L} x\right), \qquad t \geq 0, \tag{34a}$$

$$u|_{x=-L/2} = u|_{x=L/2}, \qquad t \geq 0, \tag{34b}$$

$$u = u_0, \qquad t = 0, \tag{34c}$$

where $u_0 > 0$ denotes the initial velocity (constant in the domain), L is the length of the computational domain, Δt is the time-step size used in the simulation, A_F is an amplitude constant for the forcing term, $\mathbb{N}_F = \{\pm 1, \ldots, \pm N_c\}$ is a collection of integers, and σ_N is a standard Gaussian random variable (zero mean and unit variance) that is independent for each wavenumber and each time step. We set $N_c = 80$ and $A_F = \sqrt{8} \cdot 10^{-1}\, u_0^{3/2}\, L^{-1/2}$ for the numerical experiments in this section. This completes the non-dimensional description of the problem.

The choice of forcing in (34) yields, for wavenumbers below the cut-off wavenumber $\kappa_c = 2\pi N_c / L$, a $-5/3$ slope for the inertial range of the energy spectrum [3, 12, 52, 92] and thus resembles Navier-Stokes turbulence within the Burgers setting. As is customary in the literature, we use the term Burgers *turbulence* to refer to the chaotic and turbulent-like behavior featured by the solution of the Burgers equation.

3.1.2. Details of the numerical discretization

We use the hybridized DG method with various polynomial orders to discretize Eq. (34) in space. We recall that HDG, EDG, IEDG and all other schemes within the hybridized DG family reduce to the same scheme in one-dimensional problems, and there is only one type of hybridized DG method for this problem. We refer the interested reader to [61] for the details of the hybridized DG discretization of the one-dimensional Burgers equation. The stabilization parameter is $\sigma = \max\{|u_h|, |\widehat{u}_h|\}$ (i.e. $\beta = 1$) and the total number of degrees of freedom is $N_{DOF} = (P+1) \cdot \lceil 1024/(P+1) \rceil \approx 1024$, where $\lceil\ \rceil$ denotes the rounding of a positive real number to the closest larger (or equal) integer. Note this is required to obtain an integer number of elements in the computational domain. We consider the polynomial orders $P = 1, \ldots, 7$. Exact integration is used both for the Burgers flux and the forcing term. For the former, Gauss-Legendre quadrature with the required number of points to ensure exact integration of polynomials of degree $3P$ (and thus of the Burgers flux term in the hybridized DG discretization) is used. The Galerkin projection of the forcing term is integrated exactly using the analytical expressions in [52]. The backward Euler method is used for the temporal discretization so that the scheme is fully-discrete L^2 stable. The Courant number based on the initial velocity is $u_0\, \Delta t / h^* = 0.1$ and the solution is computed from the initial time $t_0 = 0$ to the final time $t_f = 8\, L/u_0$.

3.1.3. Numerical results

The time-averaged kinetic energy spectra from $t = 2\, L/u_0$ to $t = 8\, L/u_0$ for $P = 1, \ldots, 7$ are shown on the top of Figure 4. The spectra are shifted up by a factor of 4^{P-1} to allow for easier visualization. All the spectra feature an inertial range of turbulence with slope $-5/3$ up to $\log_{10}(\kappa_c\, L) = \log_{10}(2\pi N_c) \approx 2.7$, as expected from the forcing strategy adopted. After the cut-off wavenumber, a slope of -2, typical of unforced Burgers turbulence [6], takes place whenever numerical dissipation is still small enough over these wavenumbers. In all the simulations, numerical dissipation eventually becomes significant and affects the shape of the energy spectra near the grid Nyquist wavenumber $\kappa_N\, L = \pi N_{DOF} \approx 3217$; which corresponds to the right limit of the x axis.

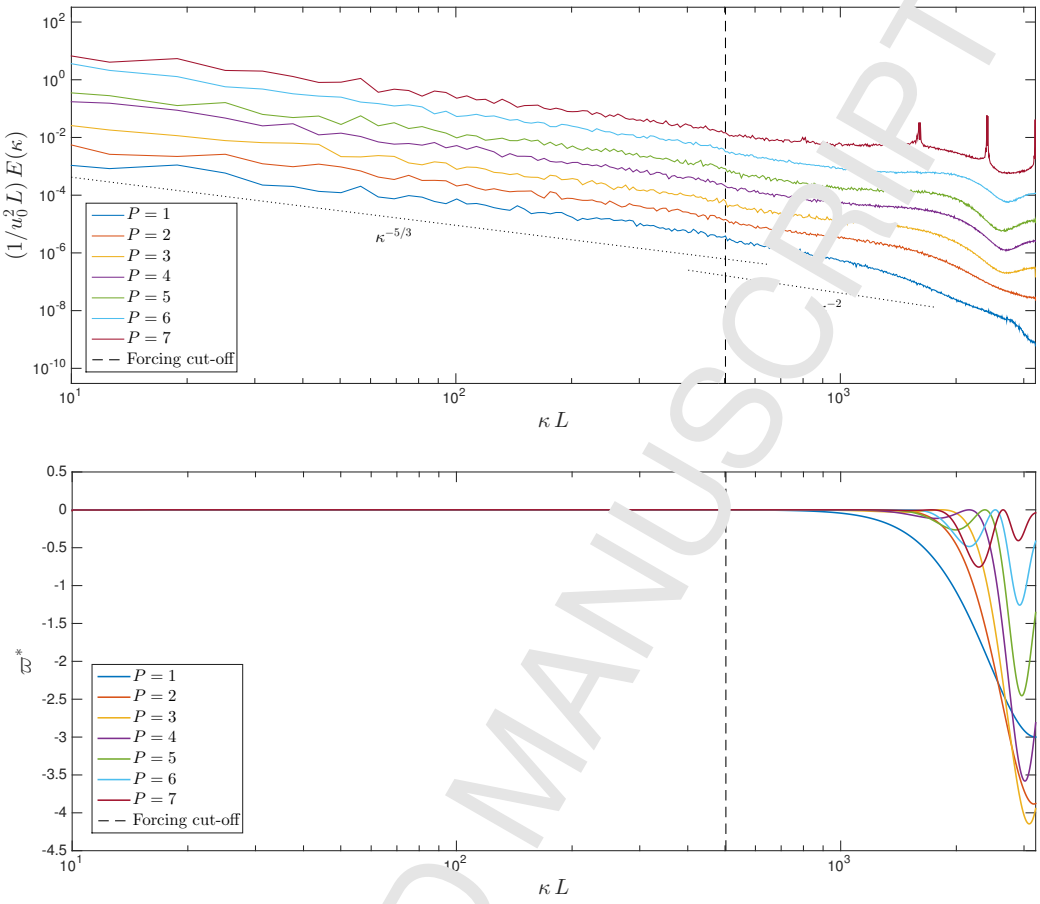

Figure 4: Results for the Burgers turbulence problem. Top: Time-averaged energy spectra from $t = 2\,L/u_0$ to $t = 8\,L/u_0$ for $P = 1, \ldots, 7$. The spectra are shifted up by a factor of 4^{P-1} to allow for easier visualization. Bottom: Short-term diffusion curves from non-modal analysis. The right limit of the x axis corresponds to the grid Nyquist wavenumber.

The short-term diffusion curves from non-modal analysis are shown on the bottom of Figure 4, where the x axis has been mapped from $\kappa\,\Delta x/(P+1)$ (as in Figures 1–3) to $\kappa\,L$ to facilitate the comparison with the energy spectra. Note that $\mathrm{Re}^* = \infty$ in this problem due to the lack of physical viscosity. The trends observed in the energy spectra are consistent with non-modal analysis results. First, a numerically induced dissipation range near $\kappa\,\Delta x = \pi$ is observed in the spectrum of the $P = \{1, 2\}$ and, to a lesser extent, $P = 3$ discretizations; which is consistent with the large short-term diffusion of these schemes right before the Nyquist wavenumber. Second, bottlenecks in the turbulence cascade (in the sense of energy accumulations at some specific wavenumbers) are observed for the high P discretizations; which is consistent with the non-monotonicity in the short-term diffusion curves. In particular, the spikes in the spectrum for $P = 7$ nearly coincide with those wavenumbers where numerical dissipation, as estimated from non-modal analysis, is approximately zero, and hints as to why instabilities can occur and high-order DG methods are usually less robust than their lower-order counterparts [29, 54, 55, 89]. Note that the results in this section differ from those obtained with standard DG in [52] since an *eigenfilter* was applied in that work to the forcing term to eliminate the effect of secondary eigenmodes, whereas now all eigenmodes contribute to the dissipation. This highlights the relevance of our non-modal analysis for large-eddy simulation and other applications where a precise eigenfilter is unfeasible.

3.2. Application to the Euler and Navier-Stokes equations. The Taylor-Green vortex

3.2.1. Problem description

The Taylor-Green vortex (TGV) problem [78] describes the evolution of the fluid flow in a three-dimensional cubic domain $\Omega = [-L\pi, L\pi)^3$ with triple periodic boundaries, starting from the smooth initial condition

$$\begin{aligned} \rho &= \rho_0, \\ u_1 &= U_0 \sin\left(\frac{x}{L}\right) \cos\left(\frac{y}{L}\right) \cos\left(\frac{z}{L}\right), \\ u_2 &= -U_0 \cos\left(\frac{x}{L}\right) \sin\left(\frac{y}{L}\right) \cos\left(\frac{z}{L}\right), \\ u_3 &= 0, \\ p &= p_0 + \frac{\rho_0 U_0^2}{16}\left(\cos\left(\frac{2x}{L}\right) + \cos\left(\frac{2y}{L}\right)\right)\left(\cos\left(\frac{2z}{L}\right) + 2\right), \end{aligned} \tag{35}$$

where ρ, p and (u_1, u_2, u_3) denote density, pressure and the velocity vector, respectively, and ρ_0, p_0, $U_0 > 0$ are some reference density, pressure and velocity magnitude. Governed by the Navier-Stokes equations (Euler equations in the inviscid case), the large-scale eddy in the initial condition leads to smaller and smaller structures through vortex stretching. For Reynolds numbers $\mathrm{Re} = \rho_0 U_0 L/\mu$ below about 1000, where μ denotes the dynamic viscosity of the fluid, the flow remains laminar at all times [9]. Above this threshold, the vortical structures eventually break down and the flow transitions to turbulence[5]. After transition, the turbulent motion dissipates all the kinetic energy, and the flow eventually comes to rest through a decay phase similar to that in decaying homogeneous isotropic turbulence, yet not isotropic here. In the high Reynolds number limit (inviscid TGV), there is no decay phase due to the lack of viscosity and the smallest turbulent scales thus become arbitrarily small as time evolves.

To investigate different Péclet numbers and flow regimes, we consider the Reynolds numbers 100, 400, 1600 and ∞. The reference Mach number is set to $\mathrm{Ma} = U_0/c_0 = 0.1$ in all cases to render the flow nearly incompressible, where c_0 denotes the speed of sound at temperature $T_0 = p_0/(\gamma - 1)\, c_v\, \rho_0$. The fluid is assumed to be Newtonian, calorically perfect, in thermodynamic equilibrium, and with Fourier's law of heat conduction and the Stokes' hypothesis. The dynamic viscosity μ is constant, the Prandtl number $\mathrm{Pr} = 0.71$ and the ratio of specific heats $\gamma = c_p/c_v = 1.4$. This completes the non-dimensional description of the problem.

3.2.2. Details of the numerical discretization

The computational domain is partitioned into a uniform $64 \times 64 \times 64$ Cartesian grid and the Embedded DG (EDG) scheme with $P = 2$ is used for the spatial discretization. The details of the EDG discretization of the Euler and Navier-Stokes equations are presented in [70]. We consider stabilization matrices of the form

$$\boldsymbol{\sigma} = \beta\, |\boldsymbol{A}_n(\widehat{\boldsymbol{u}}_h)|, \tag{36}$$

with $\beta = 0.25$ (under-upwinding) and $\beta = 1.00$ (standard upwinding), and where $\boldsymbol{A}_n = \partial(\boldsymbol{F}\cdot\boldsymbol{n})/\partial\boldsymbol{u}$ denotes the Jacobian matrix of the inviscid flux normal to the element face. We note that the stabilization matrix implicitly defines the Riemann solver in hybridized DG methods, and in particular a Roe-type solver is recovered in the case $\beta = 1.00$. The interested reader is referred to [25, Appendix A] for additional details on the relationship between the stabilization matrix and the resulting Riemann solver. Note also the scheme with $\beta = 1.00$ is linearly L^2-stable but the scheme with $\beta = 0.25$ is not [25, Appendix C], and we consider it

[5] Note that no temporal chaos (chaotic attractor) exists in the viscous Taylor-Green vortex since the flow eventually comes to rest due to viscous dissipation. We use the term *turbulence* here to refer to the phase of spatial chaos (spatial decoherence) that takes place after $t \approx 7 - 9\, L/U_0$ for Reynolds numbers above about 1000 [8].

simply to assess the agreement between non-modal analysis and nonlinear simulations for different upwinding parameters. The third-order, three-stage L-stable diagonally implicit Runge-Kutta DIRK(3,3) method [5] is used for the temporal discretization with Courant number $U_0\,\Delta t/h^* = 0.1$. The solution is computed from $t = 0$ to $t = 15\,L/U_0$.

3.2.3. Numerical results

Figure 5 shows the time evolution of one-dimensional kinetic energy spectrum at the Reynolds numbers considered. The left and right images in these figures correspond to $\beta = 0.25$ and 1.00, respectively, and the value of Pe^* at each time is indicated in the legends. The modified Péclet number in this problem is defined as $\mathrm{Pe}^* = h^*\,(\rho u)_{rms}/\mu$, where $(\rho u)_{rms}$ is the root mean square momentum. We note that, for a given Re, the Péclet number slightly changes over time due to differences in $(\rho u)_{rms}$. The short-term diffusion curves from non-modal analysis at the relevant Péclet numbers are shown in Figure 6, where the x axis has been mapped from $\kappa\,h/(P+1)$ (as in Figures 1−3) to $\kappa\,L$ to facilitate the comparison with the energy spectra, where we recall L is the characteristic length scale of the TGV domain $\Omega = [-L\pi, L\pi)^3$.

Like in Section 3.1, non-modal analysis results show good agreement with the turbulent energy spectrum in the simulations. First, energy pileups at large wavenumbers are observed in the spectrum when the short-term diffusion curves are non-monotonic and diffusion decreases after a maximum. Particularly informative is the Reynolds number 400. From non-modal analysis, the short-term diffusion curves at the corresponding $\mathrm{Pe}^* \approx 2.0 - 3.0$ are non-monotonic and monotonic near the Nyquist wavenumber with $\beta = 0.25$ and 1.00, respectively. As a consequence, energy accumulates at large wavenumbers with $\beta = 0.25$; which does not occur with standard upwinding.

Second, non-modal analysis predicts a small diffusion at high wavenumbers with under-upwinding in convection-dominated regimes, and this directly translates to the TGV results. In particular, when the physical viscosity is small (i.e. in the high Reynolds number cases), the dissipation at high wavenumbers with $\beta = 0.25$ does not suffice to dissipate all the energy that is being transferred from the larger scales through the turbulence cascade. As a consequence, and despite the diffusion curves are monotonic, energy starts to accumulate near the Nyquist wavenumber from the beginning of the simulation. As time evolves, this accumulation extends to larger scales due to the insufficient dissipation of energy at high wavenumbers, and eventually leads to nonlinear instability and the simulation breakdown at times $t \approx 4.42\,L/U_0$ and $4.01\,L/U_0$ for $\mathrm{Re} = 1600$ and ∞, respectively. In addition to non-monotonic dissipation characteristics, insufficient dissipation (specially at large wavenumbers) is *per se* another mechanism for nonlinear instability in under-resolved turbulence simulations.

4. Guidelines for the construction of robust and accurate schemes for LES

We present guidelines to improve the accuracy and robustness in LES using insights from non-modal analysis. Robust large-eddy simulations require

- Monotonic and slowly varying short-term diffusion characteristics to avoid energy bottlenecks at some specific wavenumbers.
- Sufficient dissipation near the grid Nyquist wavenumber to avoid energy accumulation at large wavenumbers.

If these two requirements are not met, numerical instabilities can develop and ultimately result in the crash of the simulation. These two requirements apply more generally to under-resolved simulations of nonlinear problems, especially problems featuring a kinetic energy cascade.

If these two conditions are met, in addition, the numerical dissipation resembles an explicit subgrid-scale model. In particular, non-modal analysis indicates that, for moderately high accuracy orders and

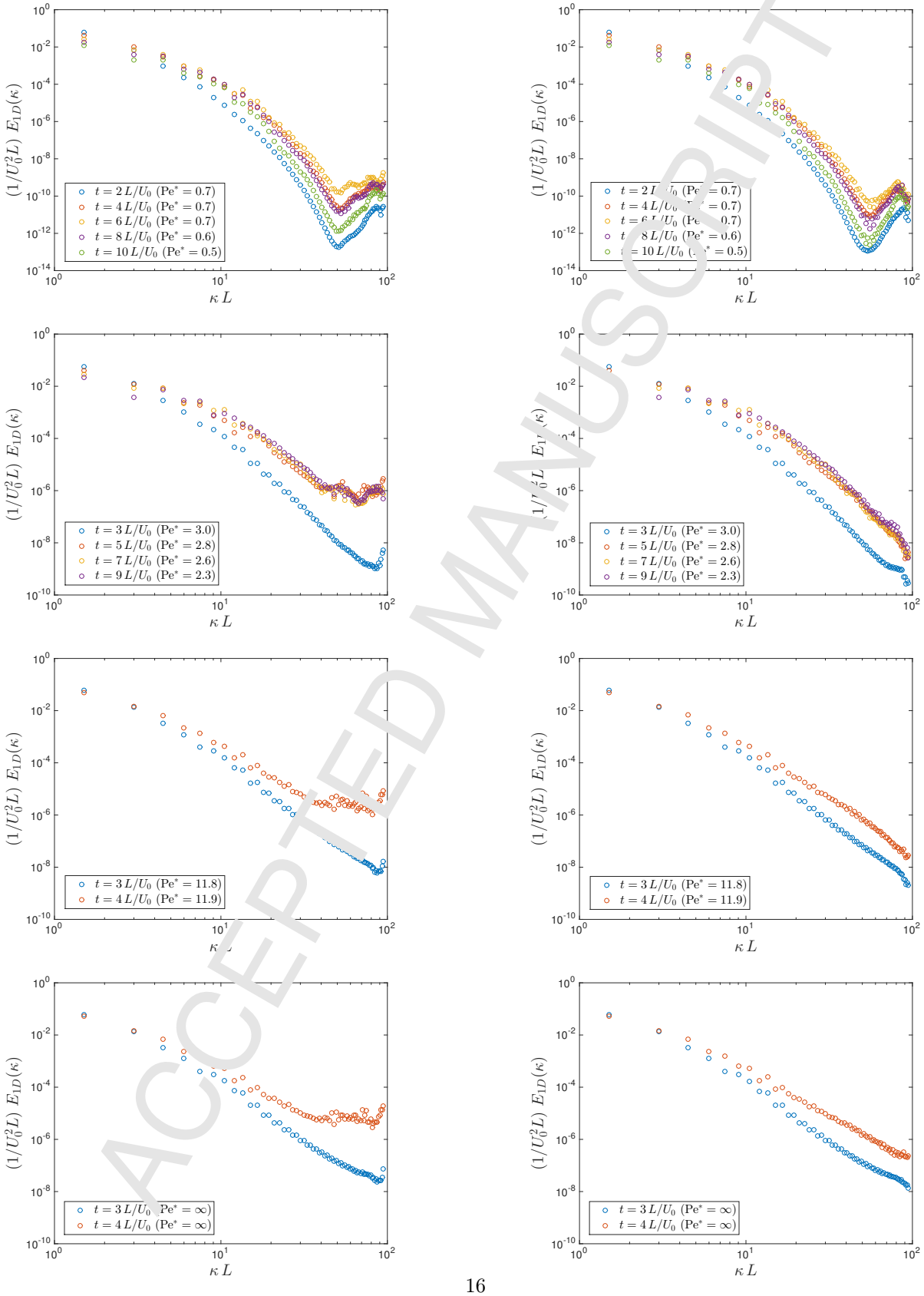

Figure 5: Time evolution of one-dimensional kinetic energy spectra for the Taylor-Green vortex at (from top to bottom) Re = 100, 400, 1600 and ∞ with $\beta = 0.25$ (left) and $\beta = 1.00$ (right). The modified Péclet number Pe* at each time is indicated in the legend. The right limit of the x axis corresponds to the grid Nyquist wavenumber.

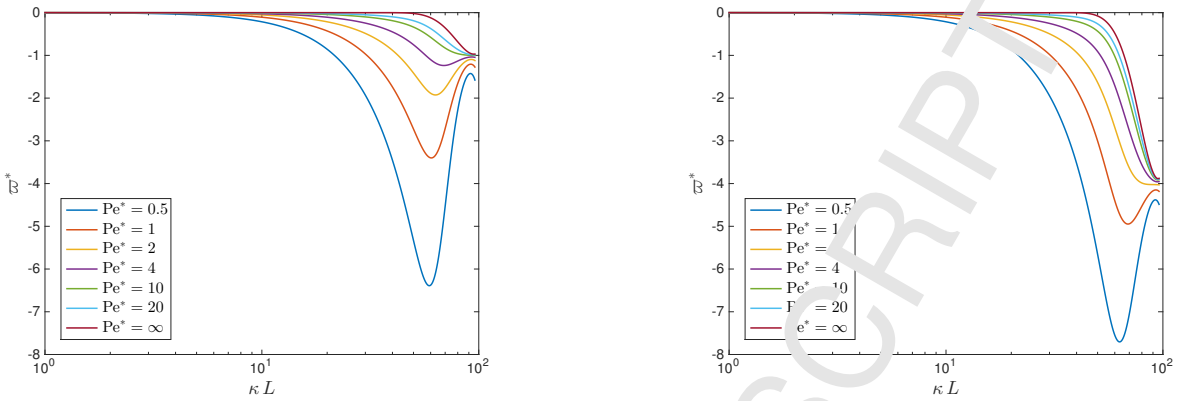

Figure 6: Short-term diffusion curves with $\beta = 0.25$ (left) and $\beta = 1.$ (right) from non-modal analysis. These curves are to be compared to the energy spectra for the Taylor-Green vortex in Figure 5. The right limit of the x axis corresponds to the grid Nyquist wavenumber.

standard upwinding, hybridized DG methods introduce numerical dissipation in under-resolved simulations of convection-dominated flows, and this dissipation is localized near the Nyquist wavenumber. This can be interpreted as an implicit subgrid-scale model similar to variational multiscale [17, 34, 35, 58], spectral vanishing viscosity [36, 37, 77] and Mori-Zwanzig [65, 66] approaches in the sense that dissipation is applied to the smallest resolved scales and the amount of dissipation depends mostly on the energy in those scales. Therefore, by choosing the element size h, the numerical flux $\widehat{f}_h$ and the polynomial order P inside of each element, the diffusion properties of the scheme can be tuned to obtain an equivalent filter width and SGS model that can be used in an implicit LES context. This information regarding diffusion properties can also be used to improve accuracy in classical (explicit) LES, by better decoupling the wavenumber of the LES filter from the dissipation introduced by the numerics.

From a non-modal analysis standpoint, and for the particular case of hybridized DG method, polynomial orders $P = 2$, 3 and 4 with standard upwinding seem to be the most adequate for LES, at least in the implicit LES context. For lower polynomial orders, dissipation is introduced at scales that are much larger than the grid resolution. Strong under/over-upwinding, as well as higher polynomial orders, may lead to numerical stability issues due to low and non-monotonic numerical diffusion. We note that Riemann solvers that are based on the maximum magnitude eigenvalue of the Jacobian matrix of the Euler fluxes, such as the Lax-Friedrichs and the HLL solvers [30], produce over-upwinding at low Mach numbers [55].

5. Conclusions

We introduced a non-modal analysis framework to investigate the short-term diffusion, in wavenumber space, of the semi-discrete system arising from the spatial discretization of the linear convection-diffusion equation. The proposed framework differs from traditional eigenanalysis techniques in that all eigenmodes are taken into account with no need to differentiate them as physical or unphysical, making practical analyses easier. While applicable to spectral element methods in general, including CG, standard DG, SD and FR methods, the non-modal analysis methodology was illustrated for the particular instance of hybridized DG methods. The effects of the polynomial order, the Péclet number and the upwinding parameter on the short-term diffusion were investigated. From these studies, and for the particular case of hybridized DG methods, the diffusion characteristics that are better suited, in terms of accuracy per DOF and robustness, for large-eddy simulation seem to be those for polynomial orders $P = 2$, 3 and, to a lesser extent, 4. Beyond these polynomial orders, the diffusion curves become strongly non-monotonic; which may lead to numerical instability due to bottlenecks in the energy spectrum. Strong under/over-upwinding, such as with

Lax-Friedrichs type Riemann solvers at low Mach numbers, may similarly lead to numerical stability and accuracy issues.

While devised in the linear setting, non-modal analysis succeeded to predict the trends observed in the nonlinear problems considered. In particular, non-modal analysis results showed excellent agreement with numerical results for the Burgers, Euler and Navier-Stokes equations. From a practical perspective, non-modal analysis gives insights on why high-order SEM may suffer from stability issues in under-resolved simulations, and on how to devise more robust schemes for these problems. Furthermore, it provides insights to understand and improve the built-in subgrid-scale model in the scheme for under-resolved turbulence simulations.

The non-modal analysis framework can be generalized in several ways. First, one may study the finite-time behavior of the system (for some fixed $t > 0$), as opposed to its short-term behavior (limit $t \downarrow 0$). The short-time behavior was considered in this paper since it is relevant to understand mechanisms that may lead to numerical instability in nonlinear problems. Second, fully-discrete formulations could be considered, with the effect of finite Courant numbers analyzed. Third, the non-modal analysis framework can be extended to arbitrary initial conditions, instead of Fourier modes only. We note, however, that Fourier modes are arguably the best choice to provide insights on the robustness and accuracy of the scheme for LES. Fourth, non-modal analysis could be extended to analyze the interactions and energy transfer between wavenumbers. Fifth, more complex discretizations, including non-uniform meshes, non-constant coefficients and multi-dimensional problems, could potentially be considered. These generalizations, however, would add more parameters to the analysis and partially defeat its purpose; which is to provide with a tool that, with a few inputs, approximately describes the behavior of the scheme for nonlinear problems.

Acknowledgments

The authors acknowledge the Air Force Office of Scientific Research (FA9550-16-1-0214) and Pratt & Whitney for supporting this effort. The first author also acknowledges the financial support from the Zakhartchenko Fellowship.

Appendix A. Connection between standard DG and hybridized DG for linear convection

In this appendix, we discuss the connections between standard DG and hybridized DG methods for pure convection. Additional details are presented in [25, Appendix A]. A discussion on the connections for pure diffusion is presented in [15, 61].

Standard DG

We consider standard DG numerical fluxes of the form

$$\widehat{f}_{h,\ominus} = a\,\frac{u_{h,\ominus} + u^L_{h,\oplus}}{2} - \beta\,|a|\,\frac{u_{h,\ominus} - u^L_{h,\oplus}}{2}, \tag{A.1a}$$

$$\widehat{f}_{h,\oplus} = a\,\frac{u_{h,\oplus} + u^R_{h,\ominus}}{2} + \beta\,|a|\,\frac{u_{h,\oplus} - u^R_{h,\ominus}}{2}, \tag{A.1b}$$

where $\beta \geq 0$ is the upwinding parameter. The cases $\beta = 0$ and $\beta = 1$ correspond to the central flux and the standard upwinding, respectively.

Hybridized DG

We consider hybridized DG numerical fluxes of the form

$$\widehat{f}_{h,\ominus} = a\,\widehat{u}_{h,\ominus} - \beta\,|a|\,(u_{h,\ominus} - \widehat{u}_{h,\ominus}), \tag{5a}$$

$$\widehat{f}_{h,\oplus} = a\,\widehat{u}_{h,\oplus} + \beta\,|a|\,(u_{h,\oplus} - \widehat{u}_{h,\oplus}). \tag{5b}$$

For $\beta > 0$, it is trivial to show that the numerical trace is uniquely defined and given by $\widehat{u}_h = (u^L_{h,\oplus} + u^R_{h,\ominus})/2$. The standard DG numerical fluxes (A.1) are therefore recovered, and both the standard and hybridized DG schemes lead to the same numerical solution u_h. We note that the hybridized DG discretization is singular for $\beta = 0$, and in particular

$$\begin{pmatrix} \delta\tilde{u}^L_h \\ \delta\widehat{u}_h \\ \delta\tilde{u}^R_h \end{pmatrix} = \begin{pmatrix} D^{-1}\tilde{\phi}_\oplus \\ 1 \\ -D^{-1}\tilde{\phi}_\ominus \end{pmatrix} \tag{A.3}$$

is in the nullspace.

References

[1] D.S. Abdi, L.C. Wilcox, T.C. Warburton, F.X. Giraldo, A GPU-accelerated continuous and discontinuous Galerkin non-hydrostatic atmospheric model, Int. J. High Perform. Comput. Appl. (2017) 1–29.

[2] D.S. Abdi, F.X. Giraldo, E.M. Constantinescu, L.E. Carr, J.C. Wilcox, T.C. Warburton, Acceleration of the IMplicit-EXplicit nonhydrostatic unified model of the atmosphere on manycore processors, Int. J. High Perform. Comput. Appl. (2017) 1–27.

[3] N. Adams, S. Hickel, S. Franz, Implicit subgrid-scale modeling by adaptive deconvolution, J. Comput. Phys. 200 (2) (2004) 412–431.

[4] M. Ainsworth, Dispersive and dissipative behaviour of high order discontinuous Galerkin finite element methods, J. Comput. Phys. 198 (1) (2004) 106–130.

[5] R. Alexander, Diagonally implicit Runge-Kutta methods for stiff ODEs, SIAM J. Numer. Anal. 14 (6) (1977) 1006–1021.

[6] J. Bec, K. Khanin, Burgers turbulence, Phys. Rep. 447 (1) (2007) 1–66.

[7] A.D. Beck, T. Bolemann, D. Flad, H. Frank, G.J. Gassner, F. Hindenlang, C.-D. Munz, High-order discontinuous Galerkin spectral element methods for transitional and turbulent flow simulations, Int. J. Numer. Meth. Fl. 76 (8) (2014) 522–548.

[8] M.E. Brachet, D.I. Meiron, S.A. Orszag, B.C. Nickel, R.H. Morf, U. Frisch, Small-scale structure of the Taylor-Green vortex, J. Fluid Mech. 130 (1983) 411–452.

[9] M.E. Brachet, Direct simulation of three-dimensional turbulence in the Taylor-Green vortex, Fluid Dyn. Res. 8 (1–4) (1991) 1–8.

[10] S. Cerutti, C. Meneveau, O.M. Knio, Spectral and hyper eddy viscosity in high-Reynolds-number turbulence, J. Fluid Mech. 421 (2000) 307–338.

[11] P. Chandrashekar, Discontinuous Galerkin method for Navier-Stokes equations using kinetic flux vector splitting, J. Comput. Phys. 233 (2013) 527–551.

[12] A. Chekhlov, V. Yakhot, Kolmogorov turbulence in a random-force-driven Burgers equation, Phys. Rev. E 51 (4) (1995) R2739.

[13] X. Chen, N.C. Nguyen, S.-H. Oh, J. Peraire, Nanogap-enhanced Terahertz sensing of 1-nm-thick dielectric films, ACS Photonics 2 (3) (2015) 417–424.

[14] A. Christophe, S. Descombes, S. Lanteri, An implicit hybridized discontinuous Galerkin method for the 3D time-domain Maxwell equations, Appl. Math. Comput. 319 (2018) 395–408.

[15] B. Cockburn, J. Gopalakrishnan, R. Lazarov, Unified hybridization of discontinuous Galerkin, mixed and continuous Galerkin methods for second order elliptic problems, SIAM J. Numer. Anal. 47 (2) (2009) 1319–1365.

[16] B. Cockburn, J. Guzman, S.C. Soon, H.K. Stolarski, An Analysis of the Embedded Discontinuous Galerkin Method for Second-Order Elliptic Problems, SIAM J. Numer. Anal. 47 (4) (2009) 2686–2707.

[17] S.S. Collis, The DG/VMS method for unified turbulence simulation, In: 32nd AIAA Fluid Dynamics Conference and Exhibit, St. Louis, USA, 2002.

[18] J.P.S. Dahm, K.J. Fidkowski, Error estimation and adaptation in hybridized discontinous Galerkin methods, In: 52nd Aerospace Sciences Meeting, National Harbor, USA, 2014.

[19] D. De Grazia, G. Mengaldo, D. Moxey, P.E. Vincent, S.J. Sherwin, Connections between the discontinuous Galerkin method and high-order flux reconstruction schemes, Int. J. Numer. Methods Fluids 75 (12) (2014) 860–877.

[20] X. Feng, P. Lu, X. Xu, A Hybridizable Discontinuous Galerkin Method for the Time-Harmonic Maxwell Equations with High Wave Number, Comput. Methods Appl. Math. 16 (3) (2016) 429–445.

[21] P. Fernandez, N.C. Nguyen, X. Roca, J. Peraire, Implicit large-eddy simulation of compressible flows using the Interior Embedded Discontinuous Galerkin method, In: 54th AIAA Aerospace Sciences Meeting, San Diego, USA, 2016.

[22] P. Fernandez, N.C. Nguyen, J. Peraire, The hybridized Discontinuous Galerkin method for Implicit Large-Eddy Simulation of transitional turbulent flows, J. Comput. Phys. 336 (1) (2017) 308–329.
[23] P. Fernandez, N.C. Nguyen, J. Peraire, Subgrid-scale modeling and implicit numerical dissipation in DG based Large-Eddy Simulation, In: 23rd AIAA Computational Fluid Dynamics Conference, Denver, USA, 2017.
[24] P. Fernandez, A. Christophe, S. Terrana, N.C. Nguyen, J. Peraire, Hybridized discontinuous Galerkin methods for wave propagation, J. Sci. Comput. (2018), In Press.
[25] P. Fernandez, Entropy-stable hybridized discontinuous Galerkin methods for large-eddy simulation of transitional and turbulent flows, PhD Thesis, Department of Aeronautics and Astronautics, Massachusetts Institute of Technology, 2018.
[26] P. Fernandez, N.C. Nguyen, J. Peraire, Entropy-stable hybridized discontinuous Galerkin methods for the compressible Euler and Navier-Stokes equations, Under review. arXiv preprint arXiv:1808.05066.
[27] P. Fernandez, N.C. Nguyen, J. Peraire, On the ability of discontinuous Galerkin methods to simulate under-resolved turbulent flows, Under review.
[28] A. Frere, K. Hillewaert, H. Sarlak, R.F. Mikkelsen, Cross-Validation of Numerical and Experimental Studies of Transitional Airfoil Performance, In: 33rd ASME Wind Energy Symposium, Kissimmee, USA, 2015.
[29] G.J. Gassner, A.D. Beck, On the accuracy of high-order discretizations for under-resolved turbulence simulations, Theor. Comput. Fluid Dyn. 27 (3) (2013) 221–237.
[30] G.J. Gassner, A.R. Winters, F.J. Hindenlang, D.A. Kopriva, The BR1 Scheme is Stable for the Compressible Navier-Stokes Equations, J. Sci. Comput. 77 (1) (2018) 154–200.
[31] G. Giorgiani, S. Fernandez-Mendez, A. Huerta, Hybridizable Discontinuous Galerkin with degree adaptivity for the incompressible Navier-Stokes equations, Comput. Fluids 98 (2014) 196–207.
[32] F. Hu, M. Hussaini, P. Rasetarinera, An analysis of the discontinuous Galerkin method for wave propagation problems, J. Comput. Phys. 151 (2) (1999) 921–946.
[33] F. Hu, H. Atkins, Eigensolution analysis of the discontinuous Galerkin method with nonuniform grids: I. One space dimension, J. Comput. Phys. 182 (2) (2002) 516–545.
[34] T.J.R. Hughes, G.R. Feijóo, L. Mazzei, J.-B. Quincy, The variational multiscale method–a paradigm for computational mechanics, Comput. Methods Appl. Mech. Engrg. 166 (1) (1998) 3–24.
[35] T.J.R. Hughes, L. Mazzei, K.E. Jansen, Large Eddy Simulation and the variational multiscale method, Comput. Visual Sci. 3 (1) (2000) 47–59.
[36] G.S. Karamanos, G.E. Karniadakis, A spectral vanishing viscosity method for large-eddy simulations, J. Comput. Phys. 163 (1) (2000) 22–50.
[37] R.M. Kirby, G.E. Karniadakis, Coarse resolution turbulence simulations with spectral vanishing viscosity large-eddy simulations (SVV-LES), J. Fluids Eng. 124 (4) (2002) 886–891.
[38] R.M. Kirby, G.E. Karniadakis, De-aliasing on non-uniform grids: algorithms and applications, J. Comput. Phys. 191 (1) (2003) 249–264.
[39] D.A. Kopriva, G.J. Gassner, An energy stable discontinuous Galerkin spectral element discretization for variable coefficient advection problems, SIAM J. Sci. Comput. 36 (4) (2014) A2076–A2099.
[40] R.H. Kraichnan, Eddy Viscosity in Two and Three Dimensions, J. Atmos. Sci. 33 (1976) 1521–1536.
[41] J. Langford, R. Moser, Optimal LES formulations for isotropic turbulence. J. Fluid Mech. 398 (1999) 321–346.
[42] C. Lehrenfeld, J. Schoberl, High order exactly divergence-free Hybrid Discontinuous Galerkin Methods for unsteady incompressible flows, Comput. Method. Appl. Mech. Eng. 307 (2016) 339–361.
[43] L. Li, S. Lanteri, N.A. Mortensen, M. Wubs, A hybridizable discontinuous Galerkin method for solving nonlocal optical response models, Comput. Phys. Commun. 219 (2017) 99–107.
[44] C. Liang, S. Premasuthan, A. Jameson, Z. Wang, Large eddy simulation of compressible turbulent channel flow with spectral difference method, In: 47th AIAA Aerospace Sciences Meeting, Orlando, USA, 2009.
[45] J. Manzanero, E. Ferrer, G. Rubio, E. Valero, On the role of numerical dissipation in stabilising under-resolved turbulent simulations using discontinuous Galerkin methods, 2018, Under review, arXiv preprint arXiv:1805.10519.
[46] G. Mengaldo, Discontinuous spectral/hp element methods: development, analysis and applications to compressible flows, PhD Thesis, Department of Aeronautics, Imperial College London, 2015.
[47] G. Mengaldo, M. Kravtsova, A.I. Ruban, S.J. Sherwin, Triple-deck and direct numerical simulation analyses of high-speed subsonic flows past a roughness element, J. Fluid Mech. 774 (2015) 311–323.
[48] G. Mengaldo, D. De Grazia, D. Moxey, P.E. Vincent, S.J. Sherwin, Dealiasing techniques for high-order spectral element methods on regular and irregular grids, J. Comput. Phys. 299 (2015) 56–81.
[49] G. Mengaldo, D. De Grazia, P.E. Vincent, S.J. Sherwin, On the connections between discontinuous Galerkin and flux reconstruction schemes: extension to curvilinear meshes, J. Sci. Comput. 67 (3) (2016) 1272–1292.
[50] G. Mengaldo, R.C. Moura, B. Giralda, J. Peiró, S.J. Sherwin, Spatial eigensolution analysis of discontinuous Galerkin schemes with practical insights for under-resolved computations and implicit LES, Comput. Fluids 169 (2018) 349–364.
[51] G. Mengaldo, D. De Grazia, R.C. Moura, S.J. Sherwin, Spatial eigensolution analysis of energy-stable flux reconstruction schemes and influence of the numerical flux on accuracy and robustness, J. Comp. Phys. 358 (1) (2018) 1–20.
[52] R.C. Moura, S.J. Sherwin, J. Peiró, Linear dispersion-diffusion analysis and its application to under-resolved turbulence simulations using discontinuous Galerkin spectral/*hp* methods, J. Comp. Phys. 298 (2015) 695–710.
[53] R.C. Moura, S.J. Sherwin, J. Peiró, Eigensolution analysis of spectral/*hp* continuous Galerkin approximations to advection-diffusion problems: Insights into spectral vanishing viscosity, J. Comp. Phys. 307 (2016) 401–422.
[54] R.C. Moura, G. Mengaldo, J. Peiró, S.J. Sherwin, An LES setting for DG-based implicit LES with insights on dissipation and robustness, In: M. Bittencourt, N. Dumont, J. Hesthaven (eds.) Spectral and High Order Methods for Partial Differential Equations ICOSAHOM 2016. Lecture Notes in Computational Science and Engineering, Vol. 119, pp. 161–

173, Springer, 2017.
[55] R.C. Moura, G. Mengaldo, J. Peiró, S.J. Sherwin, On the eddy-resolving capability of high-order discontinuous Galerkin approaches to implicit LES / under-resolved DNS of Euler turbulence, J. Comp. Phys. 330 (2017) 615–623.
[56] R.C. Moura, P. Fernandez, G. Mengaldo, J. Peraire, S.J. Sherwin, Temporal eigenanalysis of hybridized discontinuous Galerkin methods for advection-diffusion problems, J. Comp. Phys., In preparation for submission.
[57] D. Moxey, C.D. Cantwell, G. Mengaldo, D. Serson, D. Ekelschot, J. Peiró, S.J. Sherwin, R.M. Kirby, Towards p-adaptive spectral/hp element methods for modelling industrial flows, In: M. Bittencourt, N. Dumont, J. Hesthaven (eds.) Spectral and High Order Methods for Partial Differential Equations ICOSAHOM 2016. Lecture Notes in Computational Science and Engineering, Vol. 119, pp. 63–79, Springer, 2017.
[58] S.M. Murman, L.T. Diosady, A. Garai, Development of dynamic sub-grid models for variational multiscale methods, In: Proceedings of the 2014 Summer Program, Center for Turbulence Research, Stanford University, 2014.
[59] S.M. Murman, L.T. Diosady, A. Garai, M. Ceze, A Space-Time Discontinuous-Galerkin Approach for Separated Flows, In: 54th AIAA Aerospace Sciences Meeting, San Diego, USA, 2016.
[60] N.C. Nguyen, J. Peraire, B. Cockburn, An implicit high-order hybridizable discontinuous Galerkin method for linear convection-diffusion equations, J. Comp. Phys. 228 (9) (2009) 3232–3254.
[61] N.C. Nguyen, J. Peraire, B. Cockburn, An implicit high-order hybridizable discontinuous Galerkin method for nonlinear convection-diffusion equations, J. Comp. Phys. 228 (23) (2009) 8841–8855.
[62] N.C. Nguyen, J. Peraire, An Adaptive Shock-Capturing HDG Method for Compressible Flows, In: 20th AIAA Computational Fluid Dynamics Conference, Honolulu, USA, 2011.
[63] N.C. Nguyen, J. Peraire, Hybridizable discontinuous Galerkin methods for partial differential equations in continuum mechanics, J. Comput. Phys. 231 (18) (2012) 5955–5988.
[64] N.C. Nguyen, J. Peraire, B. Cockburn, A class of embedded discontinuous Galerkin methods for computational fluid dynamics, J. Comput. Phys. 302 (1) (2015) 674–692.
[65] E.J. Parish, K. Duraisamy, Non-Markovian closure models for large eddy simulations using the Mori-Zwanzig formalism, Phys. Rev. Fluids 2 (2017) 014604.
[66] E.J. Parish, K. Duraisamy, A dynamic subgrid scale model for Large Eddy Simulations based on the Mori-Zwanzig formalism, J. Comput. Phys. 349 (2017) 154–175.
[67] J.S. Park, F.D. Witherden, P.E. Vincent, High-Order Accurate Implicit Large Eddy Simulations of Flow over a NACA0021 Aerofoil in Deep Stall, AIAA J. 55 (7) (2017) 2186–2197.
[68] M. Parsani, G. Ghorbaniasl, C. Lacor, E. Turkel, An implicit high-order spectral difference approach for large eddy simulation, J. Comput. Phys. 229 (14) (2010) 5373–5393.
[69] J. Peraire, N.C. Nguyen, B. Cockburn, A hybridizable discontinuous Galerkin method for the compressible Euler and Navier-Stokes equations, In: 48th AIAA Aerospace Sciences Meeting, Orlando, USA, 2010.
[70] J. Peraire, N.C. Nguyen, B. Cockburn, An Embedded Discontinuous Galerkin Method for the Compressible Euler and Navier-Stokes Equations, In: 20th AIAA Computational Fluid Dynamics Conference, Honolulu, USA, 2011.
[71] F. Renac, M. de la Llave Plata, E. Martin, J.-B. Chapelier, V. Couaillier, Aghora: A High-Order DG Solver for Turbulent Flow Simulations, In: IDIHOM: Industrialization of High-Order Methods - A Top-Down Approach, Notes on Numerical Fluid Mechanics and Multidisciplinary Design, 128 (2015) 315–335.
[72] S. Rhebergen, B. Cockburn, A space-time hybridizable discontinuous Galerkin method for incompressible flows on deforming domains, J. Comput. Phys. 231 (11) (2012) 4185–4204.
[73] P.J. Schmid, Nonmodal Stability Theory, Annu. Rev. Fluid Mech. 39 (2007) 129–162.
[74] J. Schütz, G. May, A hybrid mixed method for the compressible Navier-Stokes equations, J. Comput. Phys. 240 (2013) 58–75.
[75] J.P. Sheldon, S.T. Miller, J.S. Pitt, A hybridizable discontinuous Galerkin method for modeling fluid-structure interaction, J. Comput. Phys. 326 (2016) 91–114.
[76] J. Slotnick, A. Khodadoust, J. Alonso, D. Darmofal, W. Gropp, E. Lurie, D. Mavriplis, CFD Vision 2030 Study: A Path to Revolutionary Computational Aerosciences, NASA/CR-2014-218178, 2014.
[77] E. Tadmor, Convergence of spectral methods for nonlinear conservation laws, SIAM J. Numer. Anal. 26 (1) (1989) 30.
[78] G.I. Taylor, A.E. Green, Mechanism of the production of small eddies from large ones, P. R. Soc. Lond. A. 158 (1937) 499–521.
[79] S. Terrana, J.-P. Vilotte, L. Guillot, A spectral hybridizable discontinuous Galerkin method for elastic-acoustic wave propagation, Geophys. J. Int. 213 (1) (2018) 574–602.
[80] E.F. Toro, Riemann Solvers and Numerical Methods for Fluid Dynamics, Springer, Berlin, 1999.
[81] L.N. Trefethen, A.E. Trefethen, S.C. Reddy, T.A. Driscoll, Hydrodynamic Stability Without Eigenvalues, Science 261 (5121) (1993) 578–584.
[82] L.N. Trefethen, Pseudospectra of Linear Operators, SIAM Rev. 39 (3) (1997) 383-406.
[83] M.P. Ueckermann, P.J. Lermusiaux, Hybridizable discontinuous Galerkin projection methods for Navier-Stokes and Boussinesq equations, J. Comput. Phys. 306 (2016) 390–421.
[84] A. Uranga, P.-O. Persson, M. Drela, J. Peraire, Implicit Large Eddy Simulation of transition to turbulence at low Reynolds numbers using a Discontinuous Galerkin method, Int. J. Numer. Meth. Eng. 87 (2011) 232–261.
[85] B. Vermeire, S. Nadarajah, P. Tucker, Canonical test cases for high-order unstructured implicit large eddy simulation, In: 52nd AIAA Aerospace Sciences Meeting, National Harbour, USA, 2014.
[86] F. Vidal-Codina, N.C. Nguyen, S.-H. Oh, J. Peraire, A hybridizable discontinuous Galerkin method for computing nonlocal electromagnetic effects in three-dimensional metallic nanostructures, J. Comput. Phys. 355 (2018) 548–565.
[87] P.E. Vincent, P. Castonguay, A. Jameson, Insights from von Neumann analysis of high-order flux reconstruction schemes,

J. Comput. Phys. 230 (22) (2011) 8134–8154.
[88] C.C. de Wiart, K. Hillewaert, Development and Validation of a Massively Parallel High-Order Solver for DNS and LES of Industrial Flows, In: IDIHOM: Industrialization of High-Order Methods - A Top-Down Approach, Notes on Numerical Fluid Mechanics and Multidisciplinary Design 128 (2015) 251–292.
[89] A.R. Winters, R.C. Moura, G. Mengaldo, G.J. Gassner, S. Walch, J. Peiró, S.J. Sherwin, A comparative study on polynomial dealiasing and split form discontinuous Galerkin schemes for under-resolved turbulence computations, J. Comput. Phys. 372 (2018) 1–21.
[90] M. Woopen, A. Balan, G. May, A hybridized discontinuous Galerkin method for three-dimensional compressible flow problems, In: 52nd AIAA Aerospace Sciences Meeting, National Harbor, USA, 2014
[91] D. Yoo, N.C. Nguyen, L. Martin-Moreno, D.A. Mohr, S. Carretero-Palacios, J. Shaver, J. Peraire, T.W. Ebbesen, S.H. Oh, High-throughput fabrication of resonant metamaterials with ultrasmall coaxial apertures via atomic layer lithography, Nano Lett. 16 (3) (2016) 2040–2046.
[92] O. Zikanov, A. Thess, R. Grauer, Statistics of turbulence in a generalized random-force-driven burgers equation, Phys. Fluids 9 (5) (1997) 1362–1367.